Int. J. Heat Mass Transfer. Vol. 36, No. 1, pp. 57–69, 1993
Printed in Great Britain

0017-9310/93 $5.00 + 0.00

Numerical simulation of melting inside a rotating cylindrical enclosure

M. PRUD'HOMME, T. HUNG NGUYEN and P. G. MAO
Département de Génie Mécanique, École Polytechnique de Montréal, C.P. 6079 A, Montréal, Québec, Canada H3C 3A7

(*Received* 30 *January* 1992 *and in final form* 24 *March* 1992)

Abstract—Melting within a rotating vertical cylinder heated at constant temperature is studied numerically. The problem is examined for a phase-change material of constant thermal properties, initially at the fusion temperature, assuming adiabatic conditions at the top and bottom of the enclosure. Natural convection and surface tension effects are neglected to study the fundamental coupling between rotation and melting. The governing equations for axisymmetric flow in the melt region are solved using computer-generated, body-fitted curvilinear coordinates, considering either a free or a no-slip boundary condition imposed at the top of the melt for a fixed bottom wall. The rotation-induced secondary flow within the cavity is found to play a role similar to that of natural convection in a non-rotating mould when the Prandtl number is of the order of one and higher, indicating a strong coupling between rotation and melting. At sufficiently high Reynolds numbers, a thermal boundary layer is formed all over the phase-change interface in the closed cavity and over its lower portion for a free surface at the top of the melt. For a low Prandtl number, coupling is weak, the interface remains straight and both the main and secondary flows are confined to a boundary layer at the rotating cylinder.

1. INTRODUCTION

IT IS NOW a well-documented fact that the phase-change of materials inside moulds can be greatly affected by convection, either free or forced, within the melt. Considerable experimental evidence has confirmed that convection influences the phase-change rate as well as the shape and progression of the solid–liquid interface, once the process has begun. In particular, the solidification of molten metals has received special attention over the past 20 years or so, since the final grain structure of a metal is largely determined during the solidification of the melt [1]. The investigations of several workers on this subject clearly showed that the crystalline structure of the solidified metals is strongly dependent upon fluid flow history in the melt pool, regardless of whether the fluid was set into motion by free [2–4] or mixed free and forced convection [5–7].

In particular, Vivès [8] examined the influence of a forced Couette flow during the solidification of superheated tin in a mould made out of a pair of concentric cylinders. The flow was driven by the rotating outer cylinder. His investigations were restricted to the examination of the main hydrodynamic and thermal parameters directly related to the crystal structure of the solidified tin. He reported the existence of an unexpected secondary flow at the bottom of the mould, similar to that produced by strong natural convection, which he suspected to be a wall effect. However, the exact nature of this flow was not immediately clear under his experimental conditions, for which the ratio Gr/Re^2 was of the order of 10, indicating a rather dominant natural convection mode. It turned out that this secondary flow, and not the primary Couette flow, was responsible for the diminution of the average grain diameter observed over most of the cross-section area of the metal samples, except near the outer radius, where the tangential velocity was important in the melt and the subsequent grain structure of the metal radically different.

The general problem of fluid flow between two rotating cylinders, including as a special case the famous Taylor problem, is of great theoretical and practical interest and has received a lot of attention so far [9]. On the other hand, comparatively little work has been done on the process of phase-change between rotating cylinders [8, 10, 11]. One of the potential applications of this set-up would be the control of crystal growth in a microgravity environment. The actual phase-change process of a metal between rotating cylinders is quite complex and experimental measurements are hard to perform. Hydrodynamic instabilities can occur, among other things, if the inner cylinder is rotating faster than a critical angular speed. The present study would like to address more specifically the question of exactly how the secondary flow is generated in a rotating cylindrical enclosure and what are the most important parameters to consider if one is mainly interested in the overall phase-change effects, such as the melting rate as a function of the speed of rotation, the cylinder aspect ratio and the Prandtl number. For this purpose, let us consider the phenomenon in an enclosure similar to that of Vivès, that is, with a fixed bottom, in which solidification is replaced by the melting of a solid at the fusion temperature. There is then no heat conduction in the solid and the flow problem can be solved separately.

NOMENCLATURE

a^{ij}	contravariant components of the metric tensor ($a^{11}=\xi_r^2+\xi_z^2$; $a^{12}=\xi_r\eta_r+\xi_z\eta_z$; $a^{22}=\eta_r^2+\eta_z^2$)
c	specific heat [J kg^{-1} K^{-1}]
f	scalar function
g	gravity [m s^{-2}]
J	Jacobian, $r_\xi z_\eta - z_\xi r_\eta$
k	thermal conductivity [J s^{-1} m^{-1} K^{-1}]
l	latent heat of fusion [J kg^{-1}]
L	cylinder height [m] or aspect ratio
n	normal direction at the liquid–solid boundary
$\hat{\mathbf{n}}$	unit vector along the normal (n_r, n_z)
Nu	local Nusselt number
p	dynamic pressure [Pa]
Pe	Peclet number, $Re\,Pr$
Pr	Prandtl number, ν/α
r	coordinate [m]
Re	Reynolds number, $\Omega r_0^2/\nu$
t	time [s]
T	temperature [°C]
$\mathbf{u}$	velocity vector, (u, v, w) [m s^{-1}]
U^1, U^2	contravariant velocity components in the ξ, η plane
z	coordinate [m].

Greek symbols

α	thermal diffusivity [m^2 s^{-1}]
Γ	rv product [m^2 s^{-1}]
ε	Stefan number, $c(T_0-T_f)/l$
η	transformed coordinate
θ	angular coordinate
ν	kinematic viscosity [m^2 s^{-1}]
ξ	transformed coordinate
ρ	density [kg m^{-3}]
τ	dimensionless time
ϕ, φ	parameters
ψ	stream function [m^2 s^{-1}]
ω	vorticity vector, (ω_r, ω_θ, ω_z) [s^{-1}]
Ω	angular velocity [s^{-1}].

Subscripts and superscripts

f	value at the liquid–solid interface
i, j	integers
0	value at the outer cylinder.

Other symbols

∇	gradient
$\nabla\cdot$	divergence
∇^2	Laplacian
$\hat{\nabla}^2$	transformed Laplacian
,	derivative.

In order to study the pure coupling between the rotation-induced secondary flow and melting, natural convection and surface tension effects will not be considered at all. The effect of having either a free surface at the top of the melt or a fixed wall will be examined. The influence of the Prandtl number will be assessed by comparing the results obtained for the case of a low value, corresponding to that of tin at melting point, and a relatively high value, corresponding to that of water at room temperature.

2. MATHEMATICAL FORMULATION

The geometry of the problem is shown schematically in Fig. 1. The liquid melt is assumed to be an incompressible fluid of constant thermal properties. Only the forced, axisymmetric convection flow driven by the outer rotating cylinder is being studied here, leaving aside any buoyancy-induced motions within the molten material. If a free surface is considered at the top of the melt, it is assumed to remain flat at all times and to be free of surface tension effects. Neglecting viscous heating, the appropriate form of the governing equations will be

$$\nabla\cdot\mathbf{u}=0 \tag{1}$$

$$\frac{\partial\mathbf{u}}{\partial t}+(\mathbf{u}\cdot\nabla)\mathbf{u}=-\frac{\nabla p}{\rho}+\nu\nabla^2\mathbf{u} \tag{2}$$

$$\frac{\partial T}{\partial t}+(\mathbf{u}\cdot\nabla)T=\alpha\nabla^2 T. \tag{3}$$

The no-slip boundary condition applies for the velocity vector components $u(r,z)$, $v(r,z)$ and $w(r,z)$,

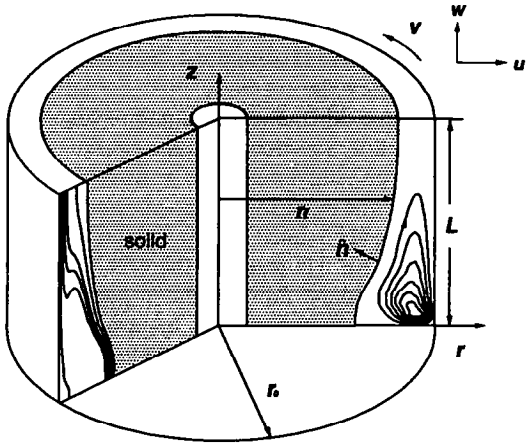

FIG. 1. Geometry and coordinate system.

which are required to vanish at all the solid boundaries, except at $r = r_0$, where the v component is given by

$$v = \Omega r_0; \quad r = r_0. \tag{4}$$

When a free surface is present at $z = L$, the no-slip condition is relaxed for a no-shear condition yielding

$$\frac{\partial u}{\partial z} = \frac{\partial v}{\partial z} = w = 0; \quad z = L. \tag{5}$$

The temperature field $T(r, z)$ must satisfy in any case

$$T = T_0; \quad r = r_0 \tag{6a}$$

$$T = T_f; \quad r = r_f \tag{6b}$$

$$\frac{\partial T}{\partial z} = 0; \quad z = 0, L. \tag{6c}$$

The pressure field may be eliminated in the usual way by taking the curl of the momentum equation (2), which leads to the transport equation

$$\frac{\partial \omega}{\partial t} + (\mathbf{u}\cdot\nabla)\omega - (\omega\cdot\nabla)\mathbf{u} = \nu\nabla^2\omega \tag{7}$$

for the vorticity vector ω. The θ component of this equation is given by

$$\frac{\partial \omega_\theta}{\partial t} + u\frac{\partial \omega_\theta}{\partial r} + w\frac{\partial \omega_\theta}{\partial z} - \frac{u\omega_\theta}{r} - \frac{2v}{r}\frac{\partial v}{\partial z} = \nu\left(\nabla^2\omega_\theta - \frac{\omega_\theta}{r^2}\right) \tag{8}$$

where by definition

$$\omega_\theta = \frac{\partial u}{\partial z} - \frac{\partial w}{\partial r}. \tag{9}$$

This formulation makes it clear that a secondary flow must be expected in the (r, z) plane as soon as a radial vorticity component $\omega_r = -\partial v/\partial z$ is present. Vortex stretching, which is accounted for by the $(\omega\cdot\nabla)\mathbf{u}$ term in equation (7), is responsible for the appearance of $v\,\partial v/\partial z$ in equation (8), where it acts as a source term. Without this source, there cannot be any secondary flow at all.

Neither the position nor the shape of the melting front are known a priori. Nevertheless, a simple energy balance at the liquid–solid interface gives an equation from which they can be determined. Assuming that there is no density variation of the material during phase-change, the appropriate form of the equation will be

$$\rho l\frac{\partial n}{\partial t} = -k\frac{\partial T}{\partial n} \tag{10}$$

giving the required interface propagation speed at each point. The axial symmetry of the problem allows a stream function formulation for the velocity components u, w and the vorticity ω_θ itself, which may then be expressed in terms of the stream function ψ as

$$u = \frac{1}{r}\frac{\partial \psi}{\partial z} \tag{11a}$$

$$w = -\frac{1}{r}\frac{\partial \psi}{\partial r} \tag{11b}$$

$$r\omega_\theta = \nabla^2\psi - \frac{2}{r}\frac{\partial \psi}{\partial r}. \tag{11c}$$

The continuity equation (1) is then automatically satisfied, while the vorticity and stream function equations (8) and (11c) must be solved together with

$$\frac{\partial v}{\partial t} + u\frac{\partial v}{\partial r} + w\frac{\partial v}{\partial z} + \frac{uv}{r} = \nu\left(\nabla^2 v - \frac{v}{r^2}\right). \tag{12}$$

The change of variable $\Gamma = rv$ eliminates the uv term above, but before we proceed any further, it is preferable to seek a non-dimensional formulation of the problem. Introducing the appropriate dimensionless variables

$$(r, z, n)' = (r, z, n)/r_0; \quad (u, w)' = (u, w)/\Omega r_0$$
$$\tau = \varepsilon\alpha t/r_0^2; \quad \omega' = \omega_\theta/\Omega; \quad \psi' = \psi/\Omega r_0^3$$
$$T' = (T - T_f)/(T_0 - T_f); \quad \Gamma' = \Gamma/\Omega r_0^2 \tag{13}$$

and dropping the superscripts from now on, the dimensionless counterparts of equations (3), (8) and (12) may be written in compact form as follows

$$\left(\frac{\varepsilon}{Pe}\frac{\partial}{\partial \tau} + u\frac{\partial}{\partial r} + w\frac{\partial}{\partial z}\right)\begin{Bmatrix}\omega\\ \Gamma\\ T\end{Bmatrix} = \nabla^2\begin{Bmatrix}\omega/Re\\ \Gamma/Re\\ T/Pe\end{Bmatrix} + \begin{Bmatrix}S_\omega\\ S_\Gamma\\ 0\end{Bmatrix} \tag{14}$$

where the so-called source terms on the right-hand side are given by

$$S_\omega = \frac{\omega}{r}\left(u - \frac{1}{r\,Re}\right) + \frac{2}{r^3}\Gamma\frac{\partial \Gamma}{\partial z} \tag{15a}$$

$$S_\Gamma = -\frac{2}{r\,Re}\frac{\partial \Gamma}{\partial r}. \tag{15b}$$

The stream function equation (11c) is left unchanged and supplies the boundary conditions for ω. For ψ itself, the appropriate condition is simply $\psi = 0$. Meanwhile, conditions (4) for v and (6) for T become, respectively, in non-dimensional form

$$T = \Gamma = 1; \quad r = 1 \tag{16a}$$

$$T = 0; \quad r = r_f \tag{16b}$$

$$\frac{\partial T}{\partial z} = 0; \quad z = 0, L. \tag{16c}$$

The other homogeneous conditions remain identical in either form. In terms of the dimensionless variables, the interface equation (10) becomes

$$\frac{\partial n}{\partial \tau} = -\frac{\partial T}{\partial n} \tag{17}$$

which may alternatively be split into components as

$$\frac{\partial r_f}{\partial \tau} = -\frac{\partial T}{\partial n} n_r \tag{18a}$$

$$\frac{\partial z_f}{\partial \tau} = -\frac{\partial T}{\partial n} n_z \tag{18b}$$

and integrated in order to find the interface position as a function of time.

3. SOLUTION PROCEDURE

3.1. *Boundary-fitted coordinates*

The governing equations for heat and fluid flow in the melt region are solved in boundary-fitted curvilinear coordinates. Adaptive grids are computer-generated for this purpose according to the general coordinate transformation method exposed by Thompson *et al.* [12], which allows a good control of the grid points distribution within the calculation domain and ensures orthogonality on the boundaries. The transformation is achieved by solving the elliptic-type equations

$$[a^{11}(\partial^2_{\xi\xi} + \phi\partial_\xi) + 2a^{12}\partial^2_{\xi\eta} + a^{22}(\partial^2_{\eta\eta} + \varphi\partial_\eta)] \begin{Bmatrix} r \\ z \end{Bmatrix} = \begin{Bmatrix} 0 \\ 0 \end{Bmatrix} \tag{19}$$

whose solution gives the image coordinates (r_{ij}, z_{ij}) of an arbitrary grid point (ξ_i, η_j) once the boundary conditions have been specified on the contour of the rectangular domain shown in Fig. 2. These conditions are nothing but the coordinates of selected boundary points in the (r, z) plane which are assigned as images to the boundary points of the rectangular (ξ, η) domain. The above may then be solved by finite-differences in order to generate the curvilinear, boundary-fitted grid of the (r, z) plane from the uniform, rectangular grid of the (ξ, η) plane. Furthermore, as the grid point distribution must follow the continuous deformation of the flow domain, a new grid has to be generated at each time step. The position of the interface nodes at time $\tau + \Delta\tau$ is determined from their previous position at time τ. The interface nodes are prone, however, either to converge towards a single point, or to diverge too much from one another. It is advisable in these circumstances to redistribute the nodes on the interface before a new grid is generated. This is accomplished by means of an interpolation by cubic splines from which the grid point distribution on the interface, and consequently within the cavity, can be controlled at will.

3.2. *Transformed equations*

The coordinate transformation is carried out in such a way that the moving interface in the physical domain is immobilized at $\eta = 1$, so that the governing equations are solved within the fixed domain $0 < \xi < 1$, $0 < \eta < 1$ at all times during the melting process. One may pass from the (r, z) system to the (ξ, η) system by substituting $r = r(\xi, \eta, \tau)$ and $z = z(\xi, \eta, \tau)$ into the original set of equations (11c), (14) and (15). The following correspondence rules are readily established

$$f_{,r}(r, z, \tau) = f_{,\xi}\xi_{,r} + f_{,\eta}\eta_{,r} \tag{20}$$

$$f_{,z}(r, z, \tau) = f_{,\xi}\xi_{,z} + f_{,\eta}\eta_{,z} \tag{21}$$

$$f_{,\tau}(r, z, \tau) = f_{,\tau} + f_{,\xi}\xi_{,\tau} + f_{,\eta}\eta_{,\tau} \tag{22}$$

for the first-order derivatives of a scalar function f where the right-hand sides are expressed in terms of the new variables (ξ, η, τ). Let us mention that the quasi-stationary approximation made by Sparrow *et al.* [13], which neglects the second and third terms on the right-hand side of equation (22), is not of great consequence for small Stefan numbers, as Wu *et al.* have confirmed in a previous study [14].

For the advection terms, the rules of tensor calculus require that

$$uf_{,r} + wf_{,z} = U^1 f_{,\xi} + U^2 f_{,\eta}. \tag{23}$$

The components U^1, U^2 of the contravariant velocity vector in the (ξ, η) system are given by

$$U^1 = u\xi_{,r} + w\xi_{,z} = \frac{1}{rJ}\psi_{,\eta} \tag{24}$$

$$U^2 = u\eta_{,r} + w\eta_{,z} = -\frac{1}{rJ}\psi_{,\xi}. \tag{25}$$

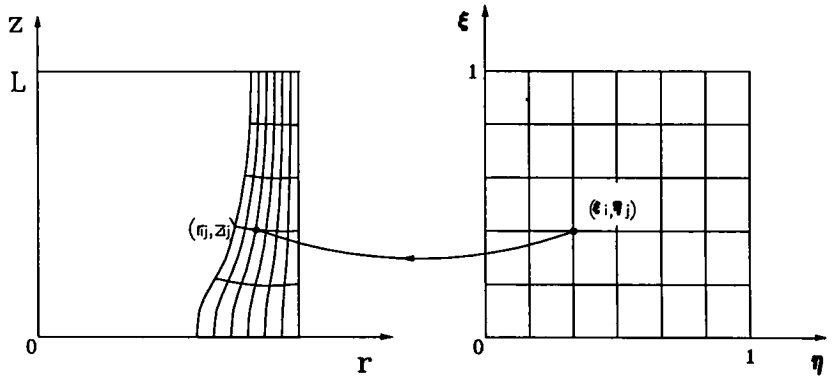

FIG. 2. Transformation of coordinates.

For the diffusion terms, the transformed Laplacian may be written after some manipulation (e.g. Prud'homme *et al.* [15]) as

$$\hat{\nabla}^2 f = a^{11}(f_{,\xi\xi} + \phi f_{,\xi}) + 2a^{12} f_{,\xi\eta} + a^{22}(f_{,\eta\eta} + \varphi f_{,\eta}) + \frac{1}{r}(f_{,\xi}\xi_{,r} + f_{,\eta}\eta_{,r}). \quad (26)$$

The original system of equations (11c), (14) and (15) may now be reformulated easily in terms of the new variables, giving

$$\left(\frac{\varepsilon}{Pe}\frac{D}{D\tau} + U^1\frac{\partial}{\partial\xi} + U^2\frac{\partial}{\partial\eta}\right)\begin{Bmatrix}\omega\\ \Gamma\\ T\end{Bmatrix} = \hat{\nabla}^2\begin{Bmatrix}\omega/Re\\ \Gamma/Re\\ T/Pe\end{Bmatrix} + \begin{Bmatrix}S_\omega\\ S_\Gamma\\ 0\end{Bmatrix} \quad (27)$$

where

$$S_\omega = \frac{\omega}{r^2}\left(\psi_{,\xi}\xi_{,z} + \psi_{,\eta}\eta_{,z} - \frac{1}{Re}\right) + \frac{2\Gamma}{r^3}(\Gamma_{,\xi}\xi_{,z} + \Gamma_{,\eta}\eta_{,z}) \quad (28a)$$

$$S_\Gamma = -\frac{2}{r\,Re}(\Gamma_{,\xi}\xi_{,r} + \Gamma_{,\eta}\eta_{,r}) \quad (28b)$$

while

$$\hat{\nabla}^2\psi - \frac{2}{r}(\psi_{,\xi}\xi_{,r} + \psi_{,\eta}\eta_{,r}) = r\omega. \quad (29)$$

On the left-hand side of equation (27), it should be remembered that

$$\frac{D}{D\tau} = \frac{\partial}{\partial\tau} + \xi_{,\tau}\frac{\partial}{\partial\xi} + \eta_{,\tau}\frac{\partial}{\partial\eta}. \quad (30)$$

It may be seen that the Stefan number appears only in front of the time derivatives. Consequently, the instantaneous flow field within the cavity is not much different from the steady-state flow in a non-deforming cavity of identical shape, as long as the Stefan number remains sufficiently small.

Boundary conditions are transformed in the same way. The rectangular contour in the (ξ, η) plane still corresponds to the streamline $\psi = 0$, whereas the no-slip condition requires that $\psi_{,\xi} = \psi_{,\eta} = 0$ everywhere except on the free surface. Since the new coordinates are orthogonal on the boundaries, equation (29) may be simplified further to supply the conditions

$$\omega = \frac{a^{11}}{r}\psi_{,\xi\xi}; \quad \xi = 0, 1 \quad (31a)$$

$$\omega = \frac{a^{22}}{r}\psi_{,\eta\eta}; \quad \eta = 0, 1 \quad (31b)$$

for vorticity, as long as the no-slip condition holds. As far as T and Γ are concerned, the set of conditions (16) becomes

$$T = 0; \quad \xi = 0 \quad (32a)$$

$$T = \Gamma = 1; \quad \xi = 1 \quad (32b)$$

$$T_{,\eta} = 0; \quad \eta = 0, 1 \quad (32c)$$

while $\Gamma = 0$ on the remaining boundaries. When the free surface is considered, the above conditions are relaxed locally for

$$\Gamma_{,\eta} = \omega = 0; \quad \eta = 1. \quad (33)$$

Finally, transforming equation (18) gives

$$r_{,\tau} = -T_{,\xi}\xi_{,r} \quad (34a)$$

$$z_{,\tau} = -T_{,\xi}\xi_{,z} \quad (34b)$$

for the melting front, which can be integrated numerically to find the position and shape of the interface at a given time.

3.3. *Numerical solution*

Numerical calculations of the flow field were carried out based on the finite-difference solution of the transformed set of governing equations in the (ξ, η) plane. The discretization process was greatly simplified by the uniform grid shown in Fig. 2. All time-dependent equations were treated according to the implicit scheme. The advection terms in equation (27) were discretized according to a second-order upwind scheme in order to ensure numerical stability during the computations, while the remaining terms were discretized according to the usual central-difference formulas for a uniform grid.

The solution algorithm selected to solve the system of discretized equations was based on the quasi-static approach, which solves separately the equations for ω, θ, Γ and ψ at each time step, and only then for the interface equation.

Calculations were started at $\tau = 0$ with zero field values for all variables except for θ_{ij} which was set equal to 1 at $\xi = 1$ and equal to 0 elsewhere. The time step was adjusted so that the molten volume would never increase by more than one per cent over a time interval of $\Delta\tau$. Computations were carried out using in most cases 15 nodes along ξ and 25 nodes along η on an IBM 3900 computer. For a typical calculation, the time step was chosen equal to $\Delta\tau = 1 \times 10^{-4}$. From 75 to 85 iterations per step are then needed on average to obtain a converged solution. The computation time required was around 10 CPU seconds per time step.

4. RESULTS

4.1. *Validation of the computer program*

In order to test the computer program, a series of Taylor vortex flow calculations were performed, for a range of parameters corresponding to those used by Meyer [16] and Alonso and Macagno [17] and the results compared against their data. In this test problem, the flow is isothermal and there is no phase-change involved at all. Consequently, the geometry under consideration is not quite as sketched in Fig. 1.

The moving interface at r_f is simply replaced by a cylinder with radius $r_i < r_0$. The boundary conditions are also reversed for the tangential velocity v, namely, the outer cylinder is held fixed and the inner cylinder is rotating, so that Taylor cells can be generated in the fluid. This classical hydrodynamic stability problem was solved using only the isothermal form of the equations, for which the Stefan and Peclet numbers are no longer relevant parameters. All the tests were done for an aspect ratio $L = 0.47$, and a radii ratio of 1.2, using an 11 by 11 uniform grid, with a time step $\Delta\tau$ of 0.1. The numerical solution procedure was found to be computationally stable in all cases, even with these coarse grids and large time steps.

Figure 3 shows the steady-state streamline pattern obtained for $Re = 2000$. A closer examination reveals that the cell pattern is symmetrical with respect to a horizontal line passing through the centre of the cavity. The four cells are similar in shape and intensity to those obtained by Meyer for $L = 0.42$ and $L = 0.50$, with the obvious difference that the present computations are carried out for an intermediate aspect ratio $L = 0.47$. It must also be pointed out that the present study assumes no-slip conditions at $z = 0$, L, corresponding to fixed end walls, instead of the periodic conditions of Meyer and Alonso. Identical results cannot be expected, therefore, as the cells are not only the product of a hydrodynamic instability, as they would be if periodic conditions were applied, but are also driven in part by pressure gradients at the top and bottom of the cavity. If the Reynolds number is set low enough, the inner pair of cells becomes weaker and eventually disappears, leaving only the convective cells at the top and bottom, which are always present regardless of how low Re is, as long as it is not zero.

How these two cells arise physically is best understood by considering the pressure field distribution

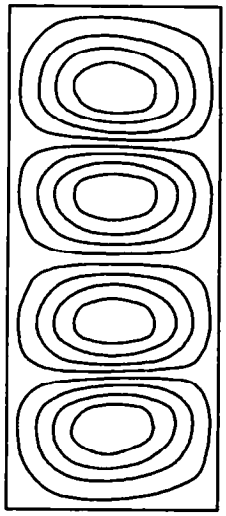

FIG. 3. Streamline configuration for test problem: $Re = 2000$, $L = 0.47$, $r_0/r_i = 1.2$.

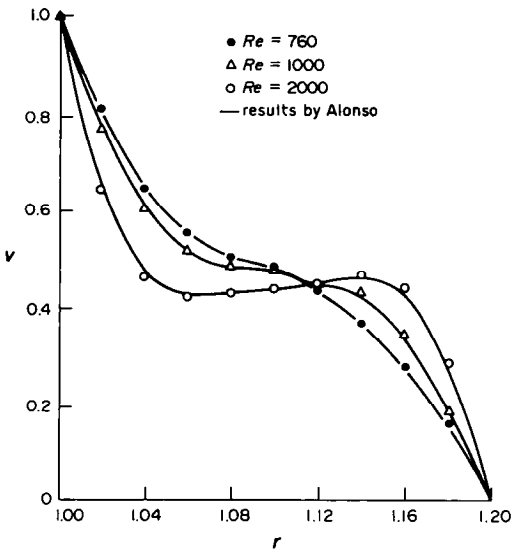

FIG. 4. Tangential velocity profiles at centre of inner vortex cell: $Re = 760$, 1000, 2000, $L = 0.47$, $r_0/r_i = 1.2$.

within the fluid. It is well known that when a streamline is curved, there must be a net pressure gradient along the normal direction to the streamline, in order to provide the centripetal acceleration of the fluid particles. Consequently, the pressure must increase here in the radial direction as a result of the streamline curvature of the main azimuthal v flow. This increase does not occur evenly along the vertical z direction, being more important in the central region of the cavity and less important near the top and bottom walls, where v is damped to zero by viscosity. A net vertical pressure gradient $\partial p/\partial z$ is thereby established which drives a secondary flow with velocity components u and w. Alternatively, one can say that viscous shear at the horizontal walls generates a radial vorticity component, which in turn drives the secondary flow through vortex stretching.

The influence of the Reynolds number on the tangential velocity is depicted next in Fig. 4, where v is plotted against r at the centre of one of the Taylor cells in the inner region of the cavity, where the pressure distribution is nearly constant in the z direction. An interesting basis for comparison is provided by the results of Alonso for $Re = 760$, 1000 and 2000. The agreement is very good indeed over most of the gap widths.

4.2. *Melting at high Prandtl numbers*

The melting process is examined first for a high-Prandtl number fluid. A value of $Pr = 7$ was chosen, which corresponds roughly to that of water at ambient temperature. Results are presented below for $Re = 140$ and 2000, at various times during melting, considering both the no-slip and free surface conditions imposed at the top of the melt. Numerical solutions were obtained for a Stefan number $\varepsilon = 0.15$ and a time step $\Delta\tau = 10^{-3}$, using an 11 by 15 grid for the low Reynolds number runs, and a 15 by 25 grid for

the high Reynolds number. The computations were started by assuming the existence of an isothermal thin melt layer, of a thickness equal to 2% of the outer cylinder radius. The temperature of this initial melt layer was set equal to the fusion temperature of the material, as mentioned before.

Figure 5(a) shows the streamline and isotherm patterns obtained within the melt for $Re = 140$. No Taylor vortices are involved in this case, since the outer cylinder is rotating and the inner boundary (the solid–liquid interface) is not, which is a stable flow configuration from the hydrodynamics point of view. The secondary flow in the (r, z) plane is driven exclusively by the vertical pressure variations discussed above. In this case, the pressure is nearly constant along the interface at $r = r_f$, while the strongest variations occur near the rotating cylinder. It is good to emphasize that this type of cell can be generated as soon as v varies in the z direction, which implies the existence of the pressure differences needed to drive the secondary flow, and does not necessarily require the action of viscosity. In fact, we were able to generate cells with free surface conditions at both $z = 0$ and L by simply choosing a conical-shaped inner boundary instead of a straight vertical cylinder.

With the no-slip conditions imposed by the fixed surface at the top and bottom, the level lines of ψ and T are perfectly symmetrical with respect to a horizontal line across the centre of the cavity, as depicted in Figs. 5(a) and (b). For the lower Reynolds number $Re = 140$, the two cells are weak at $\tau = 0.02$ and the isotherms are then nearly straight lines as they would be if there was no secondary flow at all. Conduction appears to be the dominant heat transfer mechanism across the cavity during the early stages of the process. Melting and rotation are then only weakly coupled together. The solid–liquid interface does not show any noticeable change of shape from the initial, straight vertical configuration, because the heat flux is very nearly uniform along the interface. As time goes by, however, the intensity of the cells increases and the circulating flow within the melt becomes a prominent heat transfer mechanism. The growth of the cells with the widening of the melt region results in an ever increasing number of hot fluid particles being carried out from the outer, warmer, boundary to the cooler interface along the horizontal walls, enhancing heat transfer near the top and bottom of the cavity. Melting occurs unevenly, causing a noticeable distortion of the interface after some time. This phenomenon can be seen on Fig. 5(a) at $\tau = 0.06$, in what could be called a mixed regime, where conduction remains dominant in the central region of the cavity, and convective effects are significant in the top and bottom regions. On the other hand, the streamline and isotherm patterns at $\tau = 0.12$ clearly belong to a fully convective regime, characterized by a strong coupling between rotation and melting.

For the higher Reynolds number $Re = 2000$, Fig. 5(b) shows that the interface becomes distorted much faster, as expected. The isotherm patterns reveal a new feature of the problem, that is, that thermal boundary layers are being formed at the interface, mostly in the top and bottom regions where the secondary flow is important. The calculations corresponding to $Re = 2000$ were repeated for a free surface at $z = L$, all other parameters kept constant. The zero vorticity condition at the top of the melt allowed smooth and fast convergence. The main difference with the closed cavity configuration is that there is now only the bottom surface left to drive the cells in the (r, z) plane. Consequently, symmetry is broken and there is only one cell, as can be seen in Fig. 5(c). The intensity of this single cell is also greater, since it is not competing with a second cell rotating in the opposite sense as before. The secondary flow is very similar to what would be obtained under the influence of natural convection, with the gravity vector pointing upward on the figure. Vivès [8] also noticed this similarity. His measurements, however, suggested the presence of a second cell in the melt, a clear indication of the mixed convective nature of his flow.

The evolution of the average Nusselt number at the interface for $Re = 2000$ is displayed in Fig. 6. The Nusselt number is seen to be very high at first, when the melt layer is thin and thus the temperature gradient very steep. The conductive regime is characterized by a sharp decrease of Nu as the layer becomes thicker, and is independent of the boundary condition at the top of the melt. The profiles subsequently level off at the beginning of the conductive regime and then start to decrease slowly again as the thermal boundary layers are formed. The profile corresponding to a free surface at the top of the melt is somewhat lower. The corresponding isotherm patterns of Fig. 5(c) reveal that in this case, a thermal boundary layer is formed simultaneously at the interface in the bottom region and also at the rotating surface in the top region, where it will tend to oppose heat transfer across the cavity. The growth of a boundary layer along the solidifying crust was again reported by Vivès [8] in his experiment, who, unlike in the present computations, found a greater boundary layer thickness in the bottom region. The corresponding molten volume fractions for $Re = 2000$ are plotted in Fig. 7 and compared with the pure conduction solution. If the aspect ratio L is changed while all the other parameters are kept constant, the molten volume profiles remain similar, and decreasing L increases the melting rate, since the cells cover a larger area of the cavity space for lower aspect ratios. Figure 8 shows the tangential velocity v fields at $\tau = 0.12$. On this figure, one can notice the perfect symmetry of the profile with respect to $z = 0.5$ for a fixed surface at the top of the melt and how close the profile is to solid-body rotation in the upper part of the cavity for the free surface.

4.3. *Melting at low Prandtl numbers*

The case of a low-Prandtl number fluid is considered next. The following results are presented for

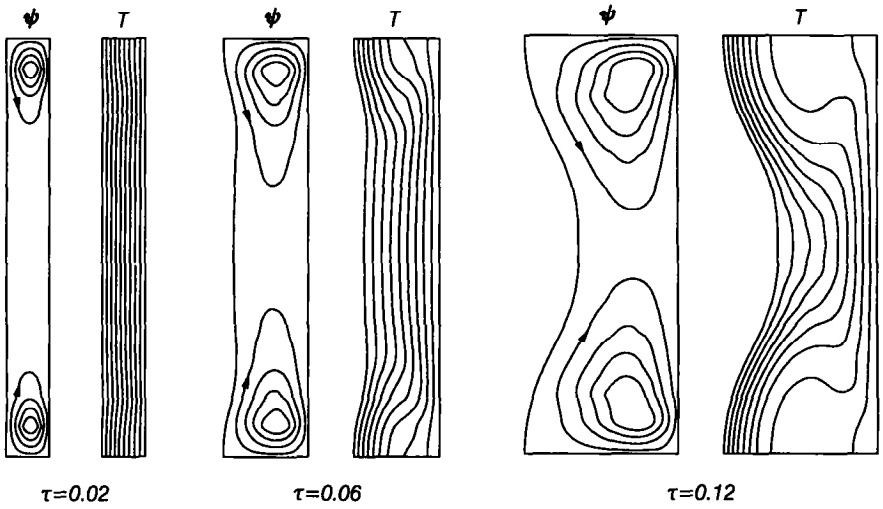

FIG. 5(a). Streamlines and isotherms: $Pr = 7$, $\varepsilon = 0.15$, $Re = 140$, $L = 2$, fixed surface at top.

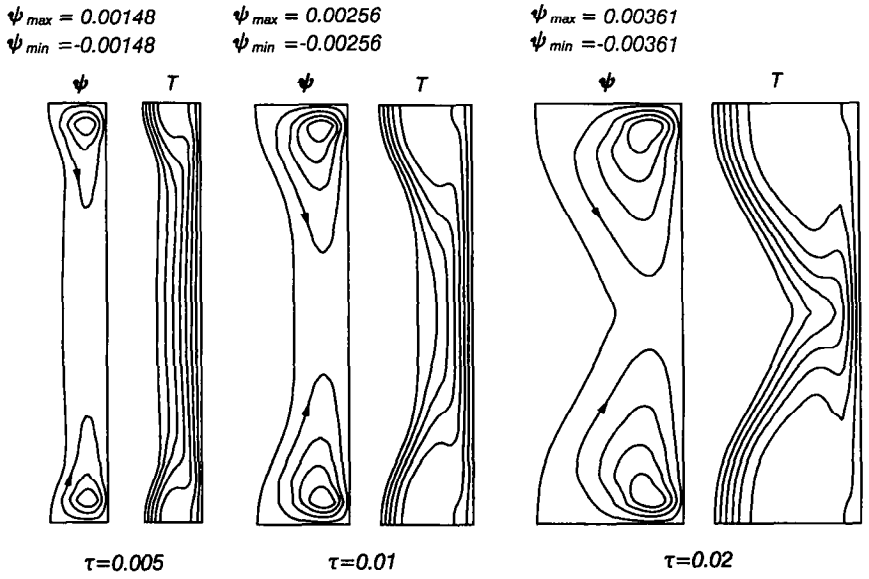

FIG. 5(b). Streamlines and isotherms: $Pr = 7$, $\varepsilon = 0.15$, $Re = 2000$, $L = 1$, fixed surface at top.

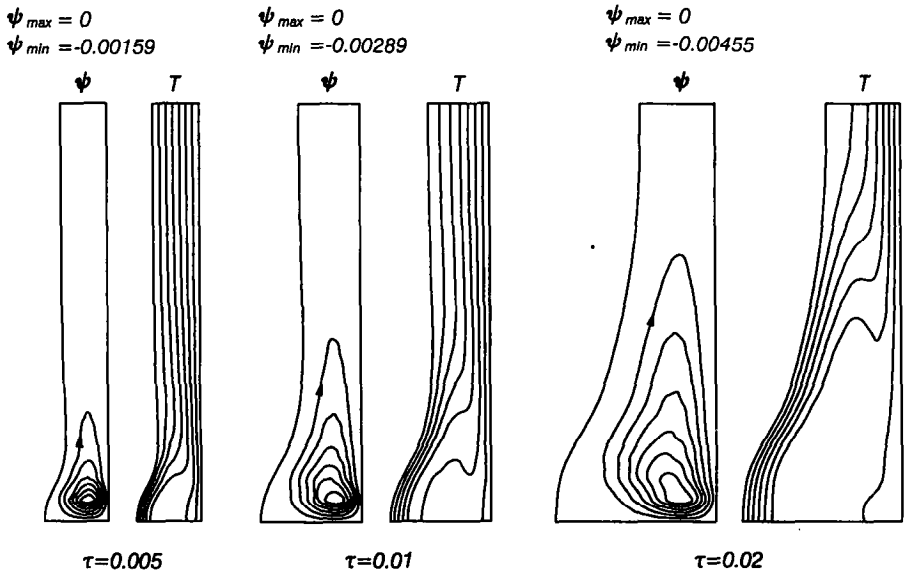

FIG. 5(c). Streamlines and isotherms: $Pr = 7$, $\varepsilon = 0.15$, $Re = 2000$, $L = 1$, free surface at top.

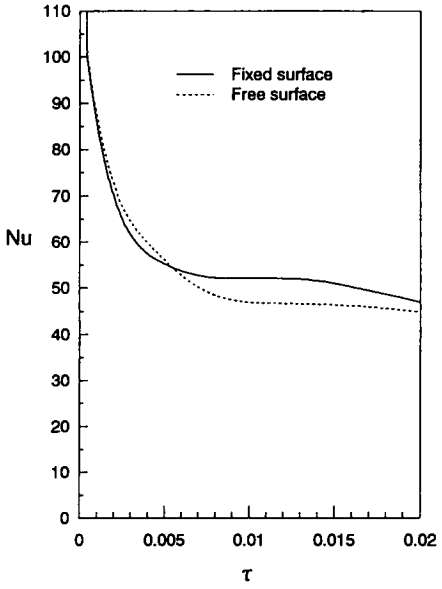

FIG. 6. Average Nusselt number at the liquid–solid interface: $Re = 2000$, $L = 1$, $Pr = 7$, $\varepsilon = 0.15$.

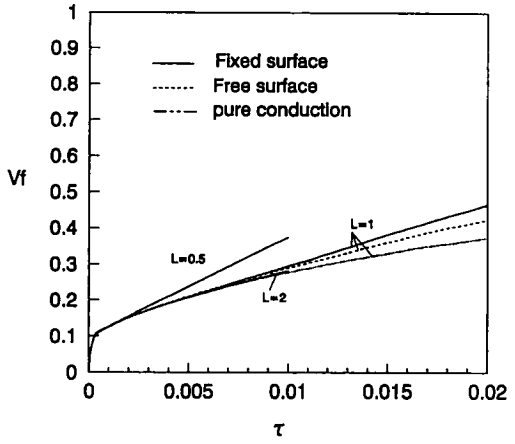

FIG. 7. Molten volume fraction: $Re = 2000$, $Pr = 7$, $\varepsilon = 0.15$.

$\varepsilon = 0.14$ and $Pr = 0.0089$, which correspond to tin at fusion temperature, as in the experiments of Vivès. All the results shown correspond to calculations done using a non-uniform 15 by 25 grid and a time step $\Delta\tau$ ranging from 10^{-4} to 5×10^{-5}, depending on the Reynolds number Re. A grid-dependence test conducted for $Re = 3 \times 10^4$ showed that using a 21 by 42 grid changed the predicted minimum and maximum values of ψ by about 1%, produced very similar streamline patterns and required four times as much computer time. Consequently, only the coarser 15 by 25 grid was used thereafter. Streamline and isotherm patterns obtained at different times are presented next.

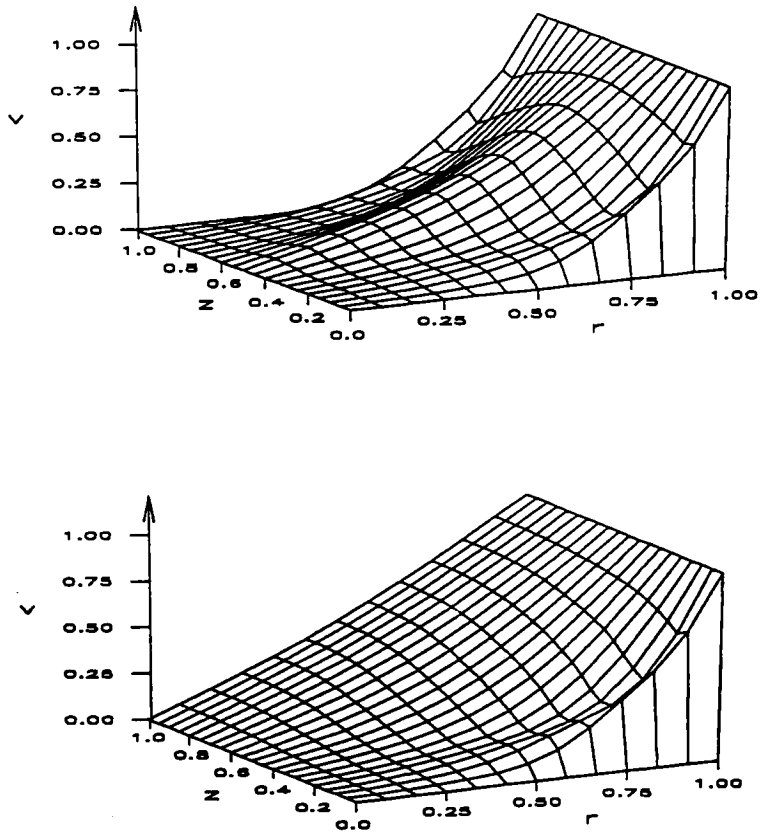

FIG. 8. Tangential velocity v at $\tau = 0.02$, $Re = 2000$, $L = 1$, $Pr = 7$, $\varepsilon = 0.15$, fixed surface (top) and free surface (bottom).

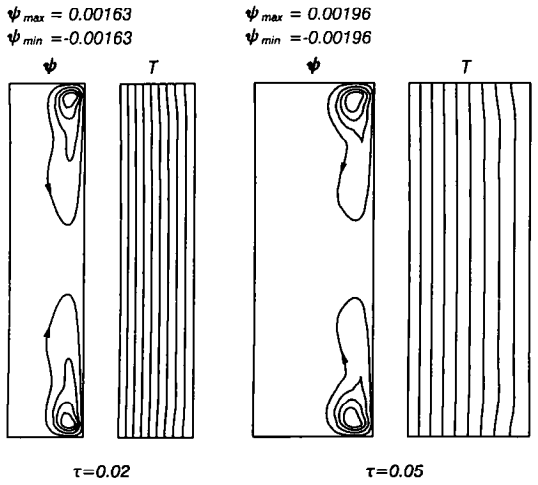

FIG. 9. Streamlines and isotherms: $Pr = 0.0089$, $\varepsilon = 0.014$, $L = 1$, $Re = 3 \times 10^4$, fixed surface.

Figure 9 shows the results for $Re = 3 \times 10^4$. Unlike what happens for $Pr = 7$, conduction remains the main heat transfer mechanism throughout the melting process, because the very low value of the Prandtl number of the fluid favours thermal diffusion over momentum diffusion by two orders of magnitude. This is expressed in analytical terms by the first terms on the right-hand side of equation (14), where $Pe = Re\ Pr$. It is then perfectly conceivable to find a situation where Re will be high enough for the flow to be nearly inviscid over a significant part of the cavity volume while, at the same time, thermal conduction will remain the foremost heat transfer mechanism. Even though convective cells are present, the interface remains nearly straight at all times. If the Reynolds number is increased up to the value of Vivès' experiment [8], that is, 2.5×10^5, the results are qualitatively similar as shown in Fig. 10. The cells remain

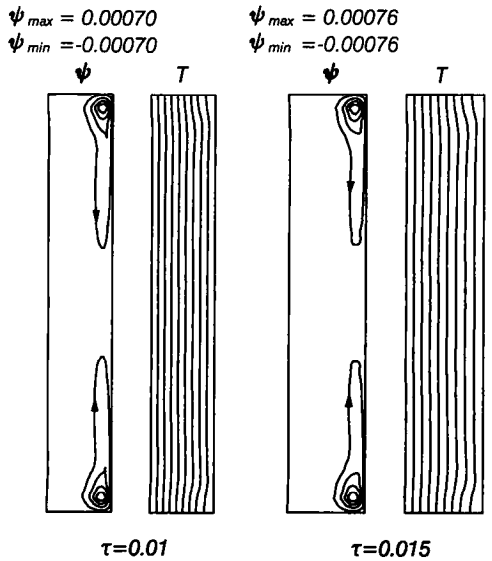

FIG. 10. Streamlines and isotherms: $Pr = 0.0089$, $\varepsilon = 0.014$, $L = 1$, $Re = 2.5 \times 10^5$, fixed surface.

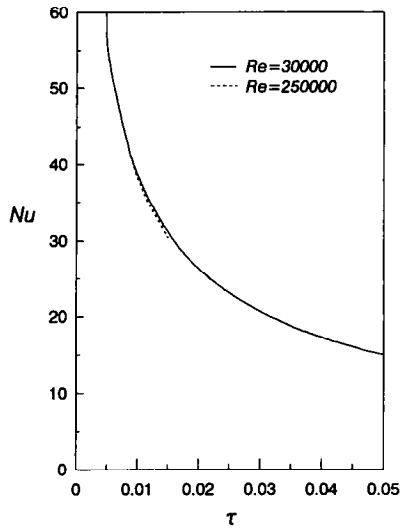

FIG. 11. Average Nusselt number at the liquid–solid interface: $Pr = 0.0089$, $\varepsilon = 0.014$, $L = 1$.

confined to a narrower region of the cavity, in what looks more and more like a boundary layer adjacent to the rotating cylinder. Unfortunately, very little work has been done so far on the transition to turbulence with the outer cylinder rotating, as mentioned by Busse *et al.* [18] and it is not possible to tell exactly when transition would normally occur in the present case. Considering the fact that the critical Reynolds number for transition to turbulence is based on the gap between the cylinders, the flow is certainly laminar at the beginning of the process, when the gap is narrow. It is known also that streamline curvature has a great influence on the intensity of turbulence, and can lead to a relaminarization of the flow under favourable conditions [19]. In a stable flow configuration such as here, this phenomenon might delay the transition for a certain period of time once melting has begun.

Average Nusselt number profiles at the interface are plotted against time in Fig. 11, for both Reynolds numbers. The simple fact that the profiles merge

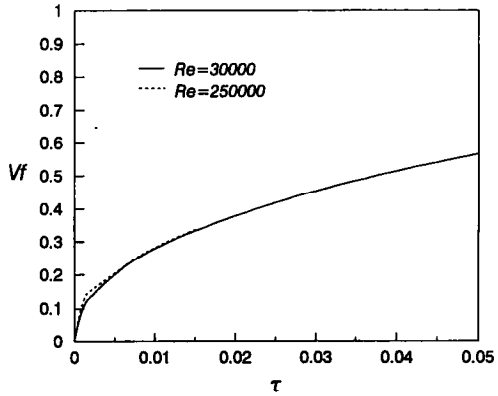

FIG. 12. Molten volume fraction: $Pr = 0.0089$, $\varepsilon = 0.014$, $L = 1$.

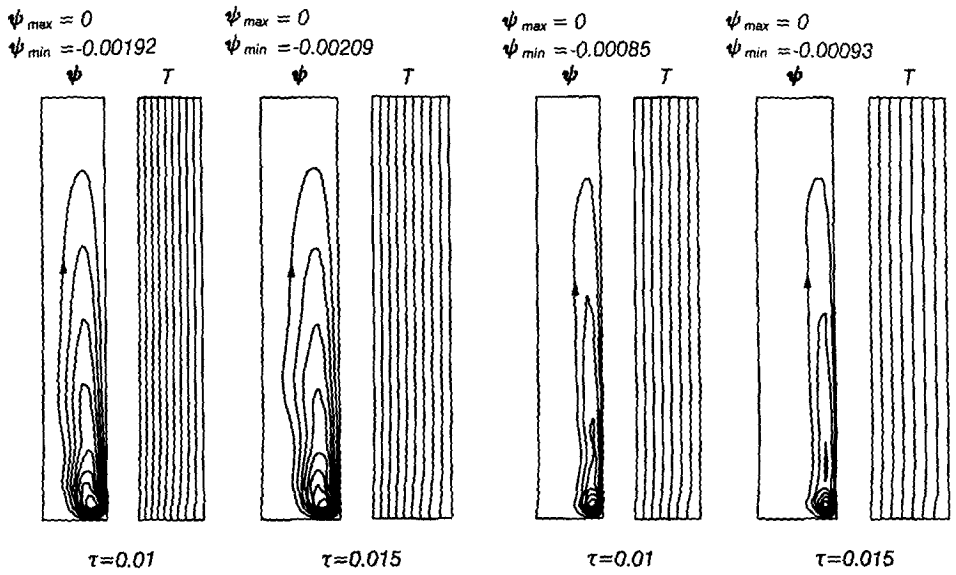

FIG. 13. Streamlines and isotherms: $Pr = 0.0089$, $\varepsilon = 0.014$, $L = 1$, free surface, $Re = 3 \times 10^4$ (left), $Re = 2.5 \times 10^5$ (right).

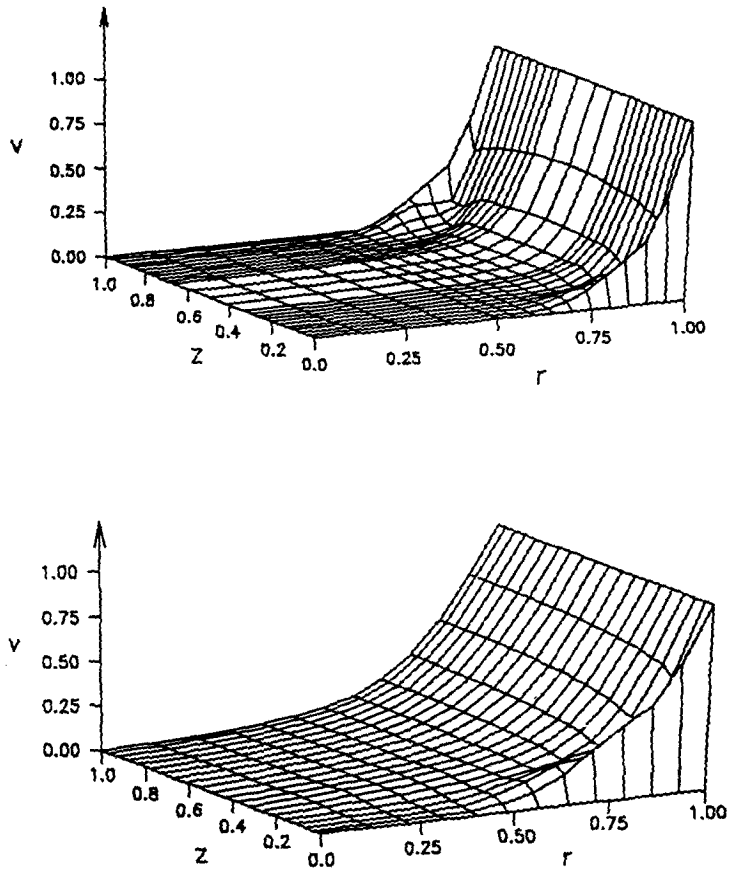

FIG. 14(a). Tangential velocity v, $Pr = 0.0089$, $\varepsilon = 0.014$, $L = 1$, $Re = 3 \times 10^4$, fixed surface (top) and free surface (bottom).

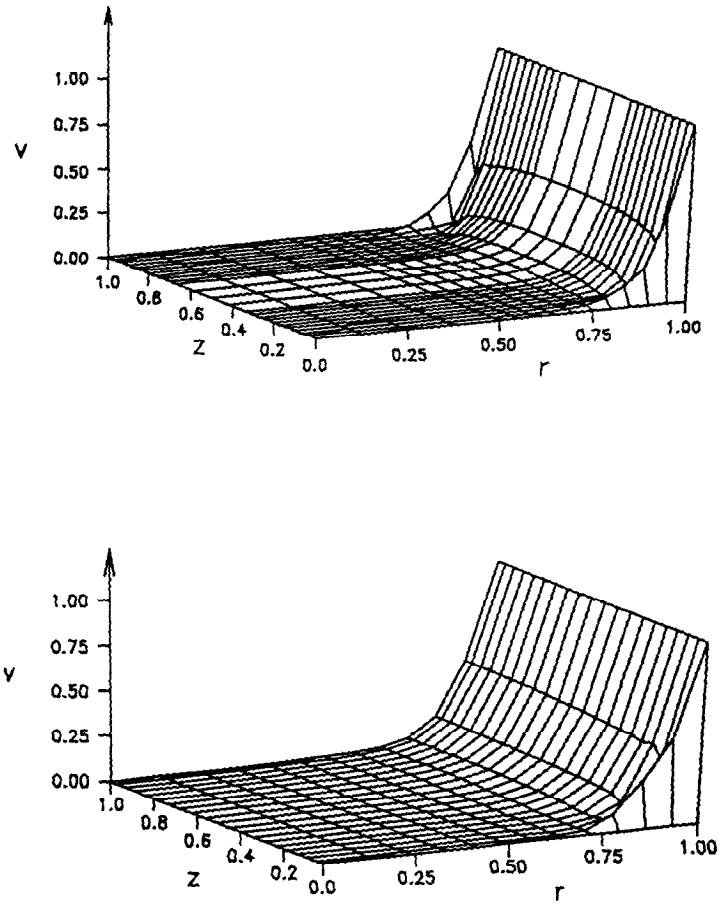

FIG. 14(b). Tangential velocity v, $Pr = 0.0089$, $\varepsilon = 0.014$, $L = 1$, $Re = 2.5 \times 10^5$, fixed surface (top) and free surface (bottom).

almost perfectly is a clear proof that Nu is virtually independent of Re or, equivalently, of the forced convection flow. The corresponding molten volume fractions are depicted in Fig. 12, vs time. Both solutions are virtually undistinguishable from the pure conduction solution.

The calculations were repeated for a free surface at $z = L$, all other parameters kept constant. Figure 13 shows the ψ and T fields obtained in this case. It is noticed that the interface remains straight as before since we used the same low Prandtl number, that is, $Pr = 0.0089$. At any given time, the single cell for $Re = 2.5 \times 10^5$ covers a greater part of the cavity volume than an individual cell of the corresponding bicellular patterns in Fig. 10, because it is always stronger. The Nusselt number and molten volume fraction profiles are not shown, since they are almost identical to those of Figs. 11 and 12. Another interesting feature of this problem is the main velocity field v. Figure 14 shows that the fluid is practically unmoved inside a core region of the cavity extending outward from the solid–liquid interface to the middle and even beyond. This finding is consistent with the fact that melting is not influenced by convection, since the velocities involved are negligible over the bulk of the melt. The v profiles are almost independent of z except, of course, near the fixed horizontal boundaries where $v = 0$. When a free surface is involved, the core region is less important. The nearly inviscid, boundary layer-type nature of the flow for large Re is made obvious in Fig. 14(b).

5. CONCLUSIONS

A secondary flow is always present in the melt, driven by vertical pressure gradients, related to uneven centripetal acceleration of the main flow due to viscous or geometrical effects. When Re is large (fast rotation), the flow is important only in the vicinity of the rotating cylindrical boundary, and the bulk of the fluid is almost at rest. For a low-Pr fluid, melting occurs by conduction, almost independently of rotation. For a moderate Pr, melting is strongly affected by the secondary flow shortly after the beginning of the process. Melting occurs much faster in this case, the solid–liquid interface becomes distorted, and thermal boundary layers may be formed locally if Re is large enough. A free surface at the top of the melt produces a single, stronger, secondary cell instead of a pair of cells and the melting rate is then slightly

lower. Regarding the melting rate, the aspect ratio of the enclosure is not an influential parameter as long as it is greater than one. When $L < 1$, melting is found to occur faster for the smaller values of L.

Acknowledgement—This work was supported by the Natural Sciences and Engineering Research Council of Canada under grants OGP626 and OGP4482.

REFERENCES

1. J. Szekely, *Fluid Flow Phenomena in Metal Processing*, p. 204. Academic Press, London (1970).
2. J. Szekely and P. S. Chabra, The effect of natural convection on the shape and movement of the melt–solid interface in the controlled solidification of lead, *Metall. Trans.* **1,** 1195–1203 (1970).
3. C. Gau and R. Viskanta, Melting solidification of a metal system in a rectangular cavity, *Int. J. Heat Mass Transfer* **27,** 113–123 (1984).
4. C. Gau and R. Viskanta, Effect of natural convection on solidification from above and melting from below of a pure metal, *Int. J. Heat Mass Transfer* **28,** 573–587 (1985).
5. H. S. Marr, Electromagnetic stirring: stepping stone to improved continuously cast products, *Iron Steel Int.* **2,** 29–41 (1979).
6. A. A. Tsavaras and H. D. Brody, Electromagnetic stirring and continuous casting-achievements, problems and goals, *J. Met.* **1,** 31–37 (1984).
7. C. Vivès and C. Perry, Effects of electromagnetic stirring during the controlled solidification of tin, *Int. J. Heat Mass Transfer* **29,** 21–23 (1986).
8. C. Vivès, Effects of a forced Couette flow during the controlled solidification of a pure metal, *Int. J. Heat Mass Transfer* **31,** 2047–2062 (1988).
9. G. Cognet, Les étapes vers la turbulence dans l'écoulement de Couette–Taylor entre cylindres coaxiaux, *J. Méc. Théor. Applic.* numéro spécial, 7–44 (1984).
10. H. K. Spitzer, M. Dubke and K. Schwerdtfeger, Rotational electromagnetic stirring in continuous casting of round strands, *Metall. Trans.* **b17,** 119–131 (1986).
11. D. B. Spencer, R. Mehrabian and M. C. Flemings, Rheological behavior of Sn-15 Pct Pb in the crystallization range, *Metall. Trans.* **3,** 1926–1932 (1972).
12. J. F. Thompson, F. C. Thames and C. W. Mastin, Automatic numerical generation of body-fitted curvilinear coordinate system for fields containing any number of arbitrary two-dimensional bodies, *J. Comp. Phys.* **15,** 299–319 (1974).
13. E. M. Sparrow, S. V. Patankar and S. Ramadhyani, Analysis of melting in the presence of natural convection in the melt region, *J. Heat Transfer* **99,** 520–526 (1977).
14. Y. K. Wu, M. Prud'homme et T. Hung Nguyen, Etude numérique de la fusion autour d'un cylindre vertical soumis à deux types de conditions limites, *Int. J. Heat Mass Transfer* **32,** 1927–1938 (1989).
15. M. Prud'homme, T. H. Nguyen et Y. K. Wu, Simulation numérique de la fusion à l'intérieur d'un cylindre adiabatique chauffé par le bas, *Int. J. Heat Mass Transfer* **34,** 2275–2286 (1991).
16. K. A. Meyer, Time dependent numerical study of Taylor vortex flow, *Physics Fluids* **10,** 1847–1879 (1967).
17. C. V. Alonso and E. O. Macagno, Numerical integration of the time-dependent equations of motion for Taylor vortex flow, *Computer Fluids* **1,** 301–316 (1973).
18. F. H. Busse, J. P. Gollub, S. A. Maslowe and H. L. Swinney, *Topics in Applied Physics*, 2nd Edn, Vol. 45, p. 289. Springer, Berlin (1985).
19. P. Bradshaw, Effects of streamline curvature on turbulent flow, *AGARDograph* 169 (1973).